minerals

MDPI

Article

Sb-Bi Alloys and Ag-Cu-Pb-Sb-Bi Sulphosalts in the Jialong Cu-Sn Deposit in North Guangxi, South China

Jianping Liu [1], Weikang Chen [1] and Qingquan Liu [2,*]

[1] Key Laboratory of Metallogenic Prediction of Nonferrous Metals and Geological Environment Monitoring, Ministry of Education, Central South University, Changsha 410083, China; liujianping@csu.edu.cn (J.L.); 18777398186@163.com (W.C.)

[2] School of Resources and Safety Engineering, Central South University, Changsha 410083, China

* Correspondence: liu_qingquan@126.com; Tel.: +86-731-888-30616

Received: 30 August 2017; Accepted: 8 January 2018; Published: 16 January 2018

Abstract: Although native bismuth is a relatively common mineral, native antimony is less abundant, and Sb-Bi alloys are relatively rare phases in Nature. Sb-Bi alloys and Ag-Cu-Pb-Sb-Bi sulphosalts have been discovered in the Jialong vein-type Cu-Sn deposit in North Guangxi, South China. The Jialong deposit is hosted by schist within the contact zone of a Neoproterozoic granite. Four stages of ore formation are recognised, with the Sb-Bi alloy- and sulphosalt-bearing assemblage formed during the third stage. Sulphosalts include Pb-Bi-Ag sulphosalts (pavonite), Sb-Bi sulphosalts (tintinaite, terrywallaceite), and Sb sulphosalt (ullmanite, freibergite, bournonite). Grains of Sb-Bi alloy measure 2–20 μm in diameter, show rounded margins and occur together with galena along the edges or internal fissures of sulphosalts. The Sb-Bi alloys do not coexist with bismuthinite, BiS (an unnamed mineral), or with native bismuth. Two phases of Sb-Bi alloys are identified based on back-scattered electron image observations and electron microprobe analysis. The textural and thermodynamic relationships indicate that Phase I was formed before Phase II. Phase I contains high Sb (69.15–80.12 wt %) and lower Bi (18.01–27.85 wt %), while Phase II contains low Sb (0.89–25.24 wt %) and high Bi (72.95–98.89 wt %). Cooling in the range of 270–400 °C and decreasing sulphur fugacity promote precipitation of Sb-Bi alloys and sulphosalts during the late stage of incursion of Sb- and Bi-bearing magmatic hydrothermal fluids.

Keywords: Sb-Bi alloys; sulphosalts; Jialong Cu-Sn deposit; south China

1. Introduction

Bismuth-bearing minerals, including native bismuth, bismuth sulphosalts, and bismuth chalcogenides, occur in a variety of deposits [1], and have attracted significant interest as a source of this useful metal. Bi and Sb are group V elements in the periodic table and occur within a range of sulphosalt minerals [2]. The complex substitution mechanisms of sulphosalts [3,4] are of particular geological interest for what they can reveal about the physico-chemical conditions of mineral formation [5–9]. Metallic Bi minerals include native bismuth, with some Pd-Bi (e.g., froodite $PdBi_2$, [10,11]) and Au-Bi (e.g., maldonite Au_2Bi, and $Au_{0.53}Bi_{0.47}$ [12]) alloys. However, Sb-Bi alloys are relatively rarely formed by geological processes.

Much of the research on Sb-Bi alloys has involved materials science applications [13]. The reported occurrences of Sb-Bi alloys include antimonian bismuth in the Loddiswell quartz carbonate vein mine, southwest England [14], the Tanco pegmatite, Canada [15], the Skrytoe scheelite skarn deposit, Russia [16] and the Katerina coal mine in the Czech Republic [17], bismuthian antimony in the Viitaniemi pegmatite, Finland [18], and from the Sulitjelma VMS-type deposit in Norway [19]. Thus,

due to their limited geologic occurrence, the composition and mineralisation conditions of Sb-Bi alloys are poorly studied.

The Jialong deposit is a small Sn-Cu deposit with metal reserves of 12,806 t Cu and 3000 t Sn [20] in North Guangxi Province, South China. This vein-type deposit is indium-bearing with abnormally high Bi and Sb contents (showing maximum Bi and Sb contents of 2010 ppm and 1155 ppm, respectively), which were observed during a recent study of indium mineralisation in the deposit (Jianping Liu' unpublished data). After further mineralogical investigation, Sb-Bi alloys and several Ag-Cu-Pb-Sb-Bi sulphosalts were discovered. Therefore, this deposit allows us to assess how Sb-Bi alloys were formed during the mineralisation processes. In this study, mineralogical analysis of ores in the Jialong Sn-Cu deposit was first performed, after which the mineral chemistry of the Sb-Bi alloys and Ag-Cu-Pb-Sb-Bi sulphosalts were obtained. We use these data to discuss the formation conditions of the Sb-Bi alloys.

2. Geological Setting

The Jialong deposit is located in the Jiuwandashan-Yuanbaoshan region (JYR) in the southwest corner of the Jiangnan Orogenic Belt (Figure 1a) [21]. The regional stratigraphy of the JYR comprises, in geochronological order, of the Paleoproterozoic Sibao Group, composed of regional low-grade metamorphic sandstone, sandy slate, phyllite, and mica schist; the Mesoproterozoic Danzhou Group, composed of metamorphic siltstone and phyllite; the Neoproterozoic Sinian sandstone, composed of siltstone and sandy slate; and Devonian limestone [22] (Figure 1b). The Sibao Group including the Yuxi, Jiuxiao and Baidingyan Formations (from top to bottom), is a thick flysch formation of hemipelagic and pelagic facies terrigenous clastic sedimentary rocks interlayered with ultramafic volcanic and intrusive rocks [23]. Granites are widespread in the JYR, intruding into the Sibao Group, and underlain by the Danzhou Group [23]. Two types of granite are identified [24]: (1) 835–820 Ma granodiorite intrusions with minimal surface outcrops; and (2) 810–800 Ma biotite granite intrusions with widespread outcrop across the district (Figures 1b and 2). Geochemical features show that the granites are strongly peraluminous S-type granites with A/CNK > 1.1, and a CIPW (Cross, Iddings, Pirsson, Washington) normative corundum content of 1.53–3.85 vol % [24]. There are more than 30 Sn-polymetallic deposits in the JYR (Figure 1b), with a total Sn reserve of 0.2 Mt [21,22]. These Sn deposits are hosted in the metamorphic rocks of the Sibao Group, and are related to type 2 granites [21].

The Jialong deposit is a vein-type deposit and is situated in the northeast of the Yuanbaoshan intrusion (Figures 1b and 2a). Contact metamorphism is local and only weakly affects the mining area. The deposit is hosted by the Yuxi Formation, which is composed of muscovite-quartz and chlorite-muscovite-quartz schist interlayered with leptinite and two-mica schist [20]. Orebodies occur in a silicified zone between the leptinite and muscovite schist of the Yuxi Formation (Figure 2a). The mineralised silicified zone is approximately 500–600 m from the granite intrusion and approximately 1 km in length and 30–50 m in width, with an inclination of 45°–60°, and a steep dip of 55°–60° [20]. Seven orebodies (Nos. 1–7) are outlined; the first three are the major orebodies. The number 3 ore-body, the largest in the deposit, is 677 m long and 3.0–4.5 m thick, extending 442 m along the dip [20]. Orebodies are layer-like, lamellar, and lenticular with grades of 0.45–0.70 wt % Cu and 0.2–0.3 wt % Sn [20]. Ore structures of the Jialong deposit comprise irregular veinlets (Figure 3a) and veins with small amounts of massive ore (Figure 3b).

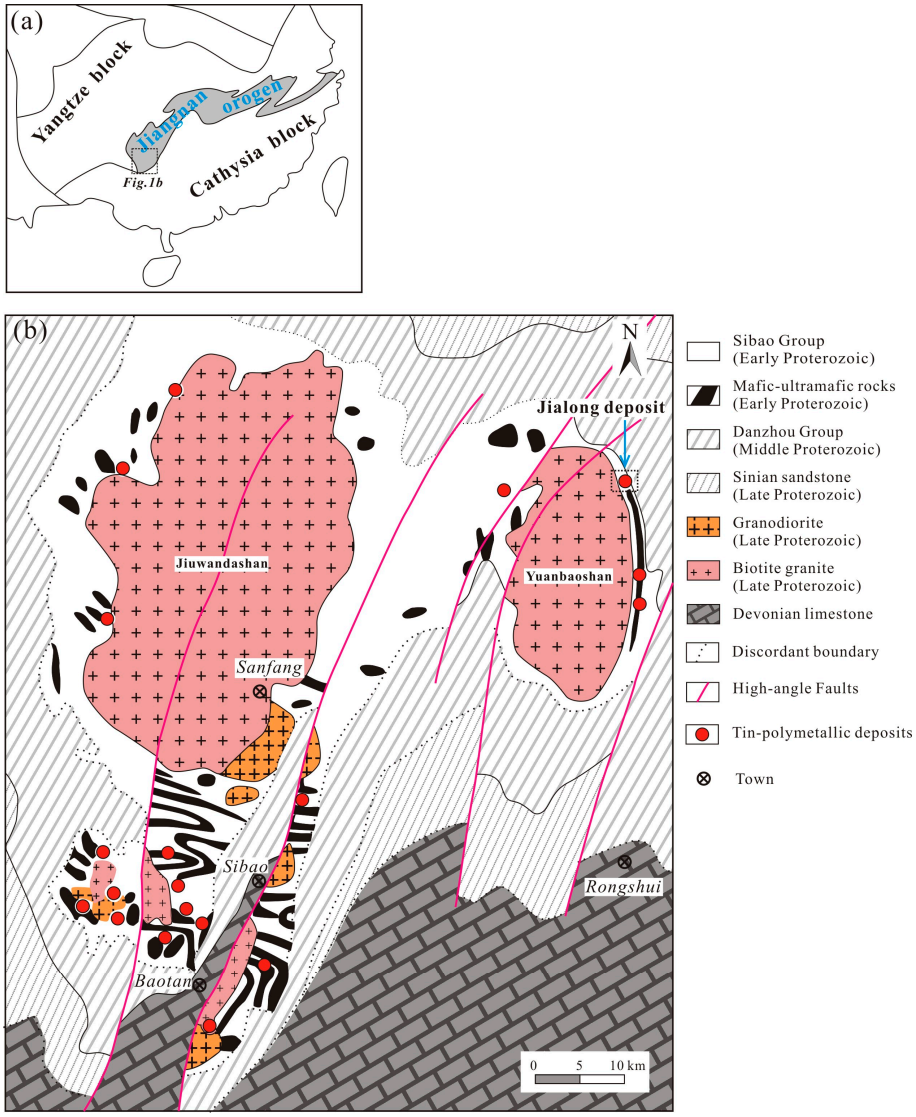

Figure 1. (**a**) Map of the tectonic units in south China (after reference [25]), showing the Jiuwandashan–Yuanbaoshan Sn-polymetallic metallogenic area located in the southwestern corner of the Jiangnan Orogen Belt; (**b**) Simplified geological map of the Jiuwandashan–Yuanbaoshan region, showing the distribution of Sn-polymetallic deposits and the location of the Jialong deposit (after reference [23]).

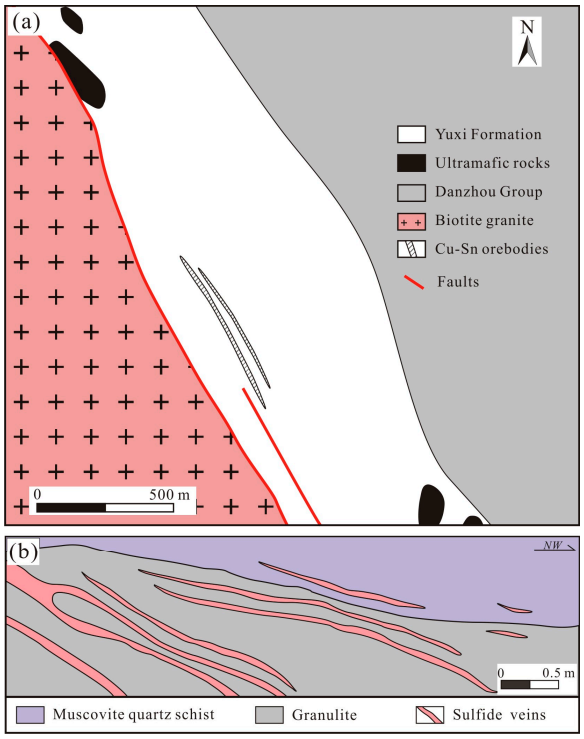

Figure 2. (**a**) Simplified geological map of the Jialong deposit (after reference [20]); (**b**) Sketch of a representative section of the vein-following drift at 440 m above sea level (after reference [20]), showing the mineralisation pattern of the Jialong deposit.

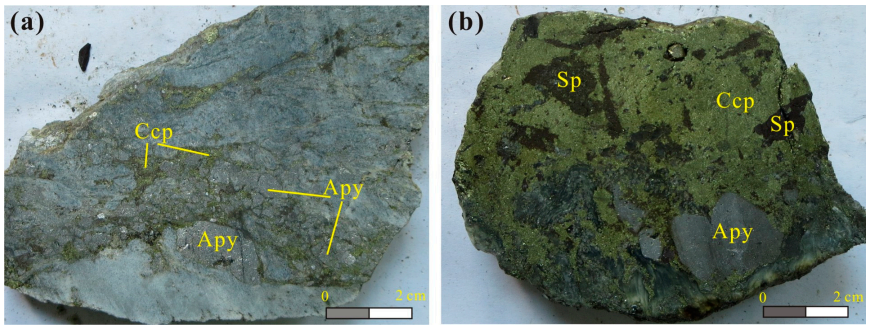

Figure 3. Photographs of typical ore samples of the Jialong deposit: (**a**) irregular chalcopyrite (Ccp) and arsenopyrite (Apy) veinlets infilling granulite; and (**b**) massive ores composed of arsenopyrite, chalcopyrite, and sphalerite (Sp).

3. Sampling and Analytical Methods

In our previous study, more than 20 ore samples were collected from the No. 3 ore-body, and 10 polished sections were prepared for microscopic observation and electron-probe microanalyses.

The ore minerals and textures were identified using standard reflected-light microscopy techniques. Analysis of chemical compositions of minerals and X-ray mapping were performed using a Shimadzu EPMA-1720H (Tokyo, Japan) electron-probe microanalyser (EPMA) housed at the School of Geosciences and Info-physics, Central South University (Changsha, China). The BSE images were obtained under 15 kV accelerating voltage and 0.5 nA beam current. Each analysis used a 15 kV accelerating voltage, a 10 nA beam current, and a 1-μm diameter electron beam. Count times were 10 seconds each for peak and background. The X-ray lines, crystals used for analysis, standards, and detection limits are listed in Table 1. The resulting data were processed using the atomic number (Z),

absorption (A), and fluorescence (F) effects (ZAF) correction method. X-ray element mapping was performed at a 15 kV accelerating voltage, and 60 nA beam current.

Table 1. Electron-probe microanalyser (EPMA) analysis conditions used in the study.

Elements	S	Fe	Ni	Cu	Zn	As	Se	Ag	Sb	Pb	Bi
X-Ray Lines	Kα	Kα	Kα	Kα	Kα	Lα	Lα	Lα	Lα	Mα	Mα
Crystals	PET	LiF	LiF	LiF	LiF	RAP	RAP	PET	PET	PET	PET
Standards	Pyrite	Pyrite	Pentlandite	Chalcopyrite	Sphalerite	Gallium arsenide	Guanajuatite	Argentite	Metal Sb	Galena	Native bismuth
Detection Limits (wt %)	0.05	0.02	0.03	0.03	0.04	0.03	0.03	0.03	0.04	0.02	0.05

4. Mineralogy and Mineral Chemistry

Based on microscopic observations and EPMA analyses, more than 27 minerals were identified. The paragenetic sequence of the minerals is summarised in Figure 4. According to mineral assemblages and crosscutting relationships, the Jialong deposit experienced four mineralisation stages (Stages I, II, III, and IV). Tourmaline, fluorite, and quartz with trace cassiterite were formed in Stage I (oxide-silicate stage). In Stage II, cassiterite, arsenopyrite, pyrite, and pyrrhotite were formed (cassiterite-sulphide stage). Next, chalcopyrite, sphalerite, stannite, Bi-, Sb-Bi-, and Sb-sulphosalts, galena I, and Sb-Bi alloys were formed in Stage III. Finally, Stage IV marks the deposition of bismuthinite, galena II, BiS (an unnamed mineral), and native bismuth.

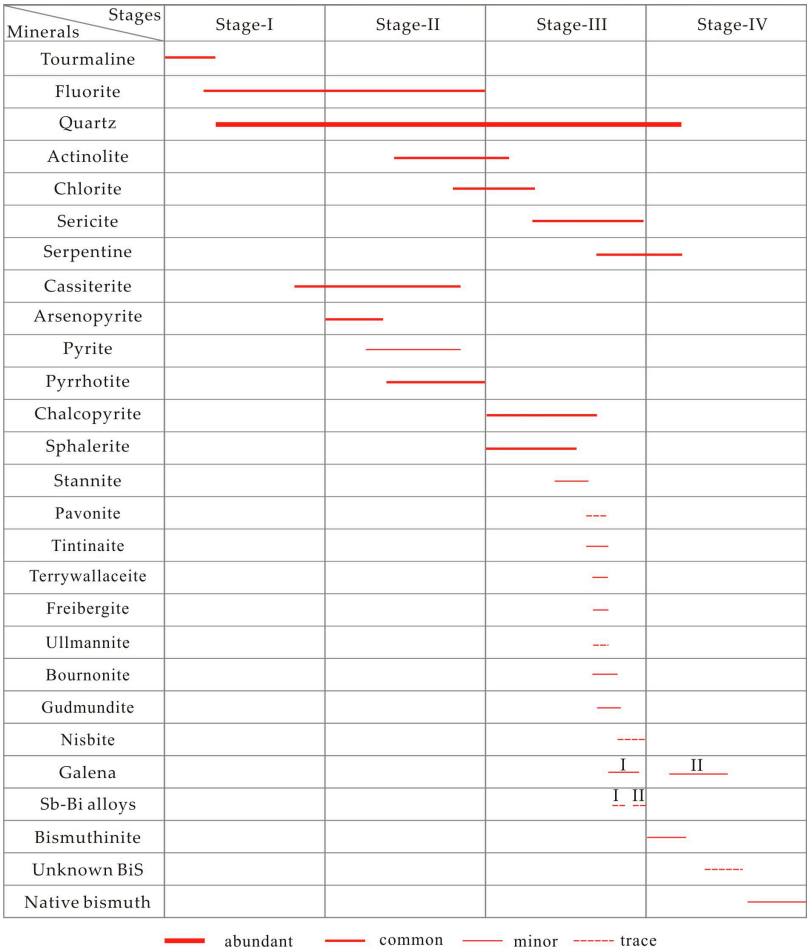

Figure 4. Paragenetic sequence of minerals observed in the Jialong deposit.

4.1. Sb-Bi Alloys and Native Bismuth

Sb-Bi alloys display intergrowth with galena and sulphosalts, but are not intergrown with bismuthinite or native bismuth. The alloys grains are small and irregular and range from 1 μm to 20 μm in diameter (Figure 5). Two phases (I and II) of Sb-Bi alloys are identified based on microscopic observations, back-scattered electron images (Figures 5 and 6), and EPMA analysis (Table 2). Phase I is accompanied by galena I (see Section 4.3 for a description of the two types of galena), tintinaite, and bournonite (Figure 6), and is replaced by Phase II (Figure 5c). Phase I contains high Sb (69.15–77.68 wt %) and low Bi (18.01–27.85 wt %), while Phase II contains low Sb (0.89–25.24 wt %) and high Bi (72.95–98.89 wt %), displaying a gap in composition. In addition, Sb-Bi alloys contain trace amounts of Cu (<0.03–1.51 wt %), Fe (0.07–1.48 wt %) and S (<0.05–0.24 wt %). We infer from mineral textures that Sb-Bi alloys formed after galena I (Figure 5a–d), and galena I formed after the sulphosalts (Figure 5d). The native bismuth comprises large grains ranging from 20–80 μm, which occur with pavonite, freibergite, galena II (see Section 4.3), and bismuthinite (Figure 7). The EPMA data shows that native bismuth is nearly pure (Table 2).

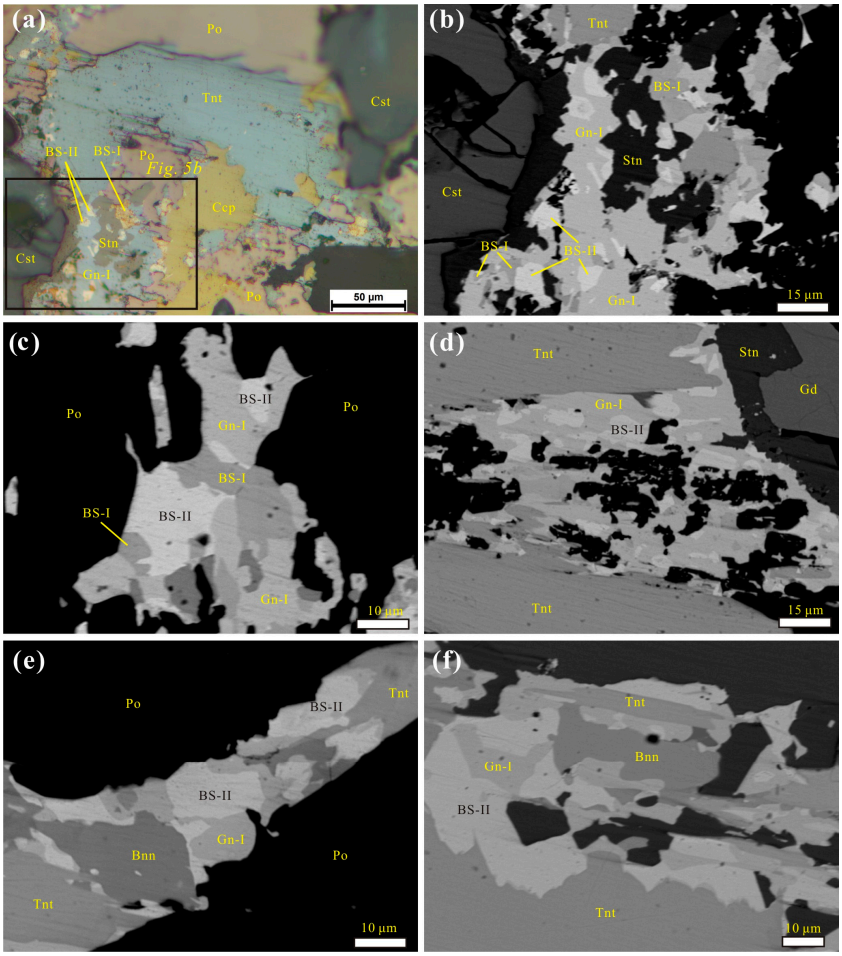

Figure 5. Reflected light photomicrograph (**a**) and back-scattered electron (BSE) images (**b**–**f**) of Sb-Bi alloys and associated minerals. (**a**) Sb-Bi alloys and galena I (Gn-I) infilling gaps between stannite (Stn) and tintinaite (Tnt), showing the different reflectance of Phase I (BS-I) and Phase II (BS-II) of the Sb-Bi alloys; (**b**) enlarged BSE image of Figure 5a, showing the different brightness of the two phases of Sb-Bi alloys; (**c**) Phase I and Phase II infilling galena I, with growth of Phase II on the irregular surfaces of Phase I; (**d**) Phase II infilling galena I, together displacing stannite and tintinaite; (**e**) Phase II of Sb-Bi alloy and galena I infill on the surface of tintinaite and bournonite (Bnn); and (**f**) Phase II and galena I deposition on the surface of tintinaite.

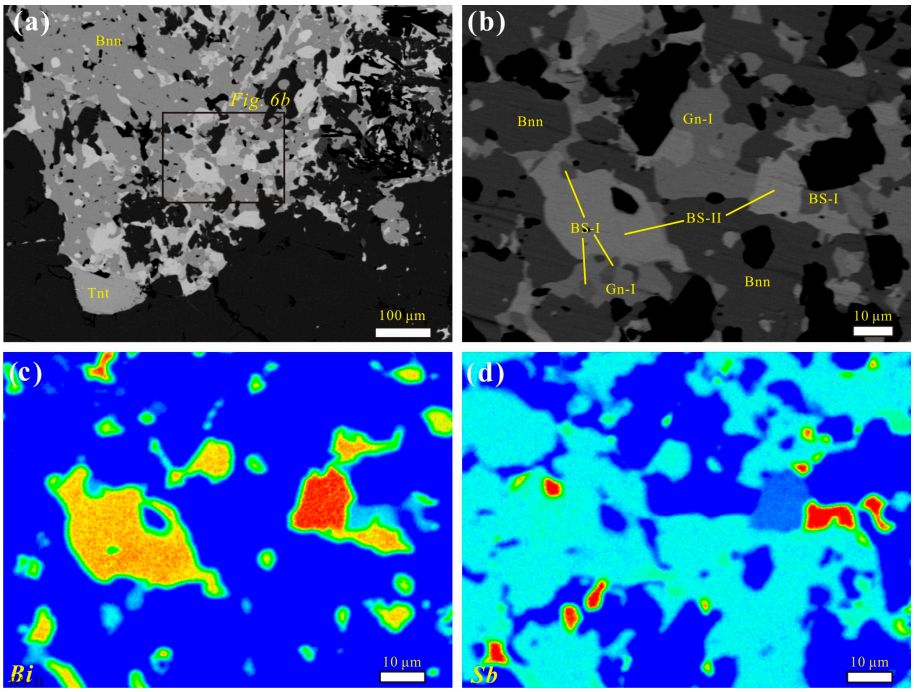

Figure 6. (**a**) Back-scattered electron images of Sb-Bi alloys and associated galena and bournonite (Bnn), showing Sb-Bi alloys and galena I infill along the edge and internal fissures of bournonite, and the later formation of Sb-Bi alloys and galena compared to bournonite; (**b**) enlarged image of Figure 6a, showing Sb-Bi alloys and galena I (Gn-I) infilling bournonite, and the different brightness of Phase I (BS-I) and Phase II (BS-II); (**c**) X-ray element-distribution map of Bi for the area of Figure 6b, showing Bi content from different Sb-Bi alloys. The Bi content of Phase I is lower than that of Phase II, and Bi content of the Phase II grains is variable; and (**d**) X-ray element-distribution map of Sb for the area of Figure 6b, showing a higher Sb content in Phase I than in Phase II.

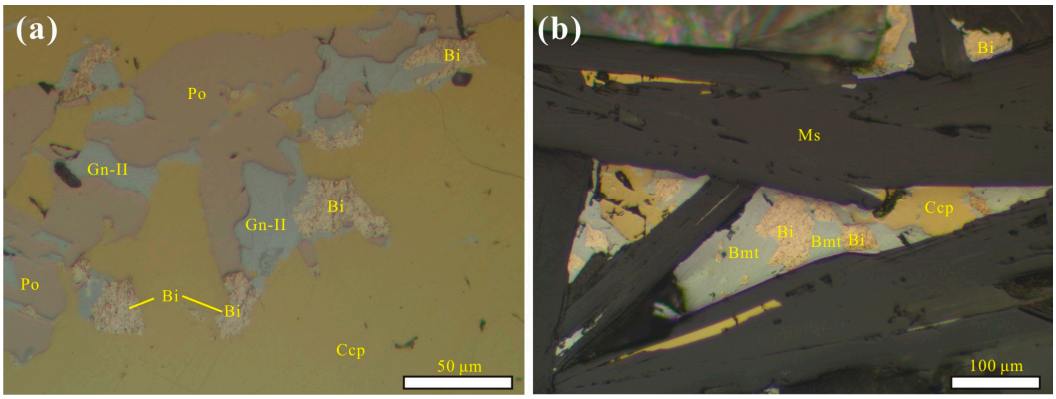

Figure 7. (**a**) Native bismuth (Bi) and galena II (Gn-II) infilling the boundaries between pyrrhotite (Po) and chalcopyrite (Ccp); and (**b**) native bismuth, bismuthinite (Bmt), and chalcopyrite infilling interstitial cavities between muscovite blades (Ms) and cleavage planes.

Table 2. EPMA data for Sb-Bi alloys and native bismuth.

Analyses	wt %									apfu Σ1 Atom							
	Cu	**Ag**	**Fe**	**Pb**	**Bi**	**Sb**	**Se**	**S**	**Total**	**Cu**	**Ag**	**Fe**	**Pb**	**Bi**	**Sb**	**Se**	**S**
Sb-Bi alloys (Phase I)																	
Bs3	0.36	-	0.36	0.85	18.01	78.66	-	0.24	98.48	0.01	-	0.01	0.01	0.11	0.85	-	0.01
Gn61	0.11	-	0.57	-	18.32	80.12	-	0.18	99.30	0.00	-	0.01	-	0.11	0.86	-	0.01
Bs13	0.20	-	0.40	-	20.29	77.68	0.04	0.12	98.73	0.00	-	0.01	-	0.13	0.85	0.00	0.00
Bs2	0.50	-	0.14	0.12	20.73	76.70	-	0.09	98.28	0.01	-	0.00	0.00	0.13	0.85	-	0.00
Bs5	0.59	-	0.07	0.14	21.47	75.64	-	0.12	98.03	0.01	-	0.00	0.00	0.14	0.84	-	0.01
Gn64	0.53	-	0.39	-	23.14	74.04	-	0.14	98.24	0.01	-	0.01	-	0.15	0.82	-	0.01
Bs11	0.10	0.04	0.49	-	23.46	73.87	-	0.14	98.10	0.00	0.00	0.01	-	0.15	0.83	-	0.01
Bs8	0.18	-	0.29	0.11	24.48	74.67	-	0.09	99.82	0.00	-	0.01	0.00	0.16	0.83	-	0.00
Gn62	0.38	-	0.16	-	24.55	72.92	-	0.07	98.08	0.01	-	0.00	-	0.16	0.82	-	0.00
Bs15	1.51	-	1.05	0.07	25.72	71.03	-	0.16	99.54	0.03	-	0.02	0.00	0.16	0.77	-	0.01
Bs12	0.17	-	0.17	0.08	27.34	70.21	0.08	0.04	98.09	0.00	-	0.00	0.00	0.18	0.81	0.00	0.00
Gn67	0.15	-	0.31	0.10	27.85	70.46	-	0.11	98.98	0.00	-	0.01	0.00	0.18	0.80	-	0.00
Bs7	0.21	-	1.48	-	27.85	69.15	-	0.14	98.83	0.00	-	0.04	-	0.18	0.77	-	0.01
Sb-Bi alloys (Phase II)																	
Gn41	0.07	-	0.23	-	72.95	25.24	0.05	-	98.54	0.00	-	0.01	-	0.62	0.37	0.00	-
Gn42	0.12	-	0.41	-	73.43	24.21	0.04	0.07	98.28	0.00	-	0.01	-	0.63	0.35	0.00	0.00
Gn59	0.20	-	0.34	-	75.21	22.47	-	0.05	98.27	0.01	-	0.01	-	0.65	0.33	-	0.00
Gn43	0.20	-	0.23	-	75.67	22.31	-	-	98.41	0.01	-	0.01	-	0.66	0.33	-	-
Gn65	0.37	-	0.19	-	76.93	22.51	-	0.08	100.08	0.01	-	0.01	-	0.65	0.33	-	0.00
Gn33	0.10	-	0.82	-	77.59	19.36	-	0.14	98.01	0.00	-	0.03	-	0.67	0.29	-	0.01
Gn66	0.36	0.09	0.65	-	77.96	20.59	-	0.13	99.78	0.01	0.00	0.02	-	0.66	0.30	-	0.01
Gn66	0.51	0.03	0.98	-	78.94	20.98	-	0.12	101.56	0.01	0.00	0.03	-	0.65	0.30	-	0.01
Gn44	0.10	-	0.16	-	79.27	19.83	-	0.05	99.41	0.00	-	0.01	-	0.69	0.30	-	0.00
Gn35	0.09	0.07	0.21	-	79.53	19.09	0.04	-	99.03	0.00	0.00	0.01	-	0.70	0.29	0.00	-
Gn40	-	-	0.65	-	80.34	17.39	-	0.10	98.48	-	-	0.02	-	0.71	0.26	-	0.01
Gn12	0.08	-	0.66	-	85.20	15.64	-	0.10	101.68	0.00	-	0.02	-	0.74	0.23	-	0.01
Gn60	0.09	0.06	0.33	-	88.19	11.60	-	0.11	100.38	0.00	0.00	0.01	-	0.80	0.18	-	0.01
Gn37	-	-	0.48	-	88.42	10.85	0.05	0.05	99.85	-	-	0.02	-	0.81	0.17	0.00	0.00
Gn30	0.54	-	0.35	-	89.24	9.94	-	0.11	100.18	0.02	-	0.01	-	0.81	0.15	-	0.01
Bs1	-	-	0.82	-	89.57	10.51	-	0.13	101.03	-	-	0.03	-	0.80	0.16	-	0.01
Gn32	0.76	-	0.78	-	91.36	8.80	-	0.10	101.80	0.02	-	0.03	-	0.81	0.13	-	0.01
Gn15	0.38	0.04	0.71	-	93.31	4.32	0.04	0.22	99.02	0.01	0.00	0.02	-	0.88	0.07	0.00	0.01
Gn29	0.16	-	0.76	-	94.27	4.37	-	0.17	99.73	0.00	-	0.03	-	0.89	0.07	-	0.01
Gn31	0.53	-	0.49	-	94.72	5.05	-	0.14	100.93	0.02	-	0.02	-	0.88	0.08	-	0.01
nBi1	0.13	-	0.24	-	96.84	3.01	-	-	100.22	0.00	-	0.01	-	0.94	0.05	-	-
nBi2	0.17	-	0.14	-	97.62	3.46	-	0.06	101.45	0.01	-	0.00	-	0.93	0.06	-	0.00
Gn72	0.06	-	0.38	-	97.83	0.96	-	-	99.23	0.00	-	0.01	-	0.97	0.02	-	-
Gn71a	0.37	-	0.24	-	98.51	1.00	-	-	100.12	0.01	-	0.01	-	0.96	0.02	-	-
Gn73	0.57	-	0.54	-	98.69	1.29	-	0.05	101.14	0.02	-	0.02	-	0.94	0.02	-	0.00
Gn84	0.31	0.04	0.23	-	98.78	1.37	0.04	-	100.77	0.01	0.00	0.01	-	0.96	0.02	0.00	-
Gn71b	0.30	-	0.20	-	98.83	0.89	-	-	100.22	0.01	-	0.01	-	0.97	0.01	-	-
Gn74	0.32	-	0.21	-	98.89	1.05	0.04	-	100.51	0.01	-	0.01	-	0.96	0.02	0.00	-
Native bismuth																	
nBi5	-	-	0.04	-	99.66	-	-	-	99.70	-	-	0.00	-	1.00	-	-	-
nBi11	-	-	0.09	-	98.69	0.05	-	-	98.83	-	-	0.00	-	1.00	0.00	-	-
nBi8	0.03	-	0.02	-	99.11	-	-	-	99.16	0.00	-	0.00	-	1.00	-	-	-
nBi9	-	-	0.03	-	99.45	-	-	-	99.48	-	-	0.00	-	1.00	-	-	-
nBi6	0.10	-	0.10	-	99.49	-	-	-	99.69	0.00	-	0.00	-	0.99	-	-	-
nBi12	-	-	-	-	100.35	-	0.04	-	100.39	-	-	-	-	1.00	-	0.00	-
nBi3	-	-	0.02	-	100.37	-	-	-	100.39	-	-	0.00	-	1.00	-	-	-
nBi13	0.05	-	-	-	100.65	-	-	-	100.70	0.00	-	-	-	1.00	-	-	-
nBi7	0.05	-	0.03	-	100.79	-	0.05	-	100.92	0.00	-	0.00	-	1.00	-	0.00	-
nBi10	-	0.04	-	-	101.01	0.05	-	-	101.10	-	0.00	-	-	1.00	0.00	-	-
Mean (n = 10)	0.06	0.04	0.05	-	99.94	0.05	0.05	-	100.19	0.00	0.00	0.00	-	0.99	0.00	0.00	-

"-" below detection limits.

4.2. Sulphosalt Minerals

Sulphosalts of the late stage-III mineralisation can be categorised as Bi-sulphosalts (pavonite), Sb-Bi-sulphosalts (tintinaite and terrywallaceite), and Sb-sulphosalts (freibergite, ullmannite, and bournonite). These minerals are discussed in the following subsections.

4.2.1. Pavonite [(Ag,Cu)(Bi,Pb)$_3$S$_5$]

Pavonite is a rare ore mineral, which occurs with galena II and native bismuth as grains of between 5 μm and 40 μm in size (Figure 8). The BSE images indicate that pavonite formed earlier than galena II and native bismuth (Figure 8b). The EPMA data (Table 3) shows that pavonite contains 67.23–70.24 wt % Bi, 11.50–12.10 wt % Ag, and 18.84–19.43 wt % S, with trace amounts of Cu (0.08–0.52 wt %), Fe (0.02–0.43 wt %), Pb (<0.02–0.43 wt %), and Se (<0.03–0.19 wt %), and an average chemical formula of $Ag_{0.95}$ $Cu_{0.03}Fe_{0.03}Bi_{2.83}$ $Pb_{0.01}S_{5.14}Se_{0.02}$.

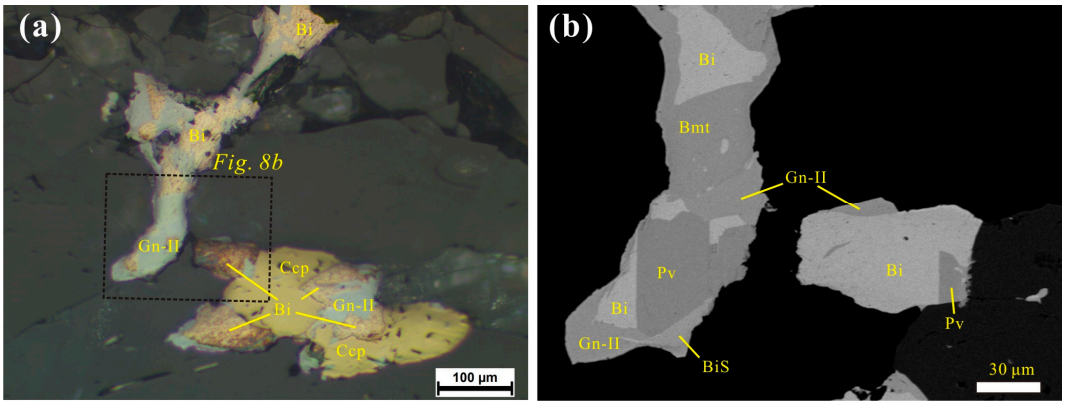

Figure 8. (**a**) Reflected light photomicrograph of pavonite (Pv) occurring with bismuthinite (Bmt), galena II (Gn-II), and native Bi. Pavonite and associated minerals occur as infilling gangue minerals; (**b**) enlarged BSE image of Figure 8a, indicating earlier formation of pavonite than galena II and native bismuth.

Table 3. EPMA data for pavonite.

Analyses	wt %									apfu ∑9 Atoms							
	Cu	Ag	Fe	Pb	Bi	Sb	Se	S	Total	Cu	Ag	Fe	Pb	Bi	Sb	Se	S
pav1	0.11	11.56	0.07	-	70.24	-	-	19.02	100.99	0.02	0.93	0.01	-	2.91	-	-	5.13
pav2	0.32	11.98	0.43	0.34	68.99	-	0.12	19.24	101.42	0.04	0.95	0.07	0.01	2.81	-	0.01	5.11
pav3	0.15	11.78	0.18	0.24	70.14	-	0.19	19.21	101.88	0.02	0.93	0.03	0.01	2.87	-	0.02	5.12
pav4	0.04	12.00	0.02	-	68.68	-	-	19.03	99.77	0.00	0.97	0.00	-	2.86	-	-	5.16
pav5	0.52	12.10	0.25	-	68.09	-	-	19.43	100.39	0.07	0.96	0.04	-	2.78	-	-	5.16
pav6	0.08	11.50	0.20	0.43	67.23	-	0.16	18.84	98.44	0.01	0.94	0.03	0.02	2.83	-	0.02	5.16
Mean (n = 6)	0.22	11.87	0.22	0.33	68.62	-	0.15	19.15	100.38	0.03	0.95	0.03	0.01	2.83	-	0.02	5.14

"-" below detection limits.

4.2.2. Tintinaite

Tintinaite is widely distributed in the Jialong ores. It predominantly occurs together with Sb-Bi alloys, and a small amount is found with native bismuth. Grains are variable in diameter, ranging from several μm to more than 500 μm, and are euhedral to subhedral (Figure 9). Tintinaite composition varies and can be divided into two types based on EPMA data (Table 4): Cu-bearing (Type-I) and Cu-poor (Type-II). Type-I contains 1.08–1.33 wt % Cu, 0.48–0.59 wt % Ag, 38.06–39.15 wt % Pb, 19.50–20.94 wt % Bi, 17.51–18.79 wt % Sb, and 19.26–19.67 wt % S. The average chemical formula, calculated on the basis of ΣS + Se = 35 at., is $Cu_{1.05}Fe_{1.64}Pb_{10.58}Ag_{0.28}$ $Bi_{5.52}Sb_{8.46}S_{34.54}Se_{0.46}$. Type-II contains <0.03–0.14 wt % Cu, 36.74–37.53 wt % Pb, 13.37–15.07 wt % Bi, 23.71–25.32 wt % Sb, and 20.87–21.71 wt % S, with an average chemical formula of $Cu_{0.04}Fe_{2.51}Pb_{9.35}Bi_{3.53}Sb_{10.67}S_{34.62}Se_{0.38}$ based on ΣS + Se = 35 at.

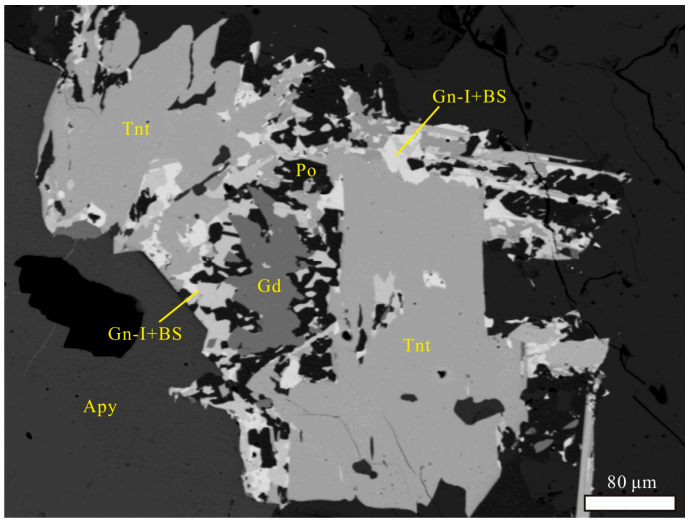

Figure 9. Back-scattered electron image showing euhedral to subhedral tintinaite crystal (Tnt) infilling arsenopyrite (Apy) and pyrrhotite (Po), and partially replaced by galena I (Gn-I) and Sb-Bi alloys along the edges and internal fissures of tintinaite and gudmundite (Gd).

Table 4. EPMA data for tintinaite.

Analyses	wt %									apfu ΣS + Se 35 Atoms							
	Cu	Fe	Pb	Ag	Bi	Sb	S	Se	Total	Cu	Fe	Pb	Ag	Bi	Sb	S	Se
Type-I																	
gn18	1.11	2.53	38.51	0.48	19.50	18.79	19.67	0.55	101.14	0.98	2.55	10.48	0.25	5.26	8.70	34.61	0.39
tnt4	1.33	1.39	39.15	0.56	19.56	18.39	19.31	0.55	100.25	1.20	1.43	10.85	0.30	5.38	8.68	34.60	0.40
Tnt5	1.08	1.44	37.85	0.59	20.94	17.54	19.26	0.74	99.45	0.98	1.48	10.48	0.32	5.75	8.26	34.46	0.54
Gn53	1.14	1.07	38.06	0.49	20.91	17.51	19.38	0.68	99.23	1.02	1.09	10.49	0.26	5.71	8.21	34.51	0.49
Mean (n = 4)	1.17	1.61	38.39	0.53	20.23	18.06	19.40	0.63	100.01	1.05	1.64	10.58	0.28	5.52	8.46	34.54	0.46
Type-II																	
tnt3	0.08	3.13	37.09	0.00	14.26	23.71	20.93	0.55	99.76	0.06	2.97	9.49	0.00	3.62	10.33	34.63	0.37
Gn27	0.07	2.50	37.53	0.00	13.37	25.08	21.25	0.38	100.17	0.06	2.35	9.50	0.00	3.35	10.80	34.75	0.25
Gn24	0.08	2.69	37.13	0.00	15.07	24.04	21.12	0.66	100.79	0.07	2.53	9.40	0.00	3.78	10.36	34.56	0.44
Gn28	0.00	2.57	37.13	0.00	13.39	25.65	21.71	0.44	100.88	0.00	2.36	9.19	0.00	3.28	10.80	34.71	0.29
Gn3	0.14	2.54	37.08	0.00	14.22	25.20	21.19	0.72	101.09	0.12	2.38	9.35	0.00	3.55	10.81	34.52	0.48
Gn1	0.03	2.66	37.03	0.00	14.28	24.69	20.87	0.67	100.23	0.03	2.53	9.49	0.00	3.63	10.76	34.55	0.45
Gn23	0.01	2.88	36.96	0.00	14.39	24.73	21.20	0.62	100.79	0.01	2.70	9.33	0.00	3.60	10.62	34.59	0.41
Gn2	0.04	2.57	36.94	0.00	13.92	25.32	21.23	0.62	100.64	0.03	2.40	9.31	0.00	3.48	10.86	34.59	0.41
Gn26	0.00	2.58	36.74	0.03	14.18	25.27	21.56	0.45	100.81	0.00	2.38	9.15	0.01	3.50	10.71	34.71	0.29
Mean (n = 9)	0.05	2.68	37.07	0.00	14.12	24.85	21.23	0.57	100.57	0.04	2.51	9.35	0.00	3.53	10.67	34.62	0.38

"-" below detection limits.

4.2.3. Terrywallaceite

Terrywallaceite is a very rare mineral that occurs in assemblages of galena II and native bismuth. Terrywallaceite was first discovered in 2011 [26], and the Jialong deposit is the first reported occurrence in China. Texturally, terrywallaceite formed earlier than galena II and native bismuth (Figure 10). EPMA data for terrywallaceite (Table 5) indicates that Pb, Ag and S contents are relatively constant (20.13–24.36 wt % Pb, 9.49–10.26 wt % Ag, 18.04–20.03 wt % S), while Bi and Sb contents are variable (27.43–41.33 wt % Bi, 8.74–19.08 wt % Sb). In addition, terrywallaceite contains trace amounts of Fe (0.15–1.13 wt %), Cu (0.04–0.96 wt %), As (0.14–0.31 wt %), and Se (0.53–1.18 wt %), with an average chemical formula of $Ag_{0.91}Pb_{1.04}Cu_{0.07}Fe_{0.10}Bi_{1.64}Sb_{1.15}As_{0.03}S_{5.96}Se_{0.10}$, similar to the ideal chemical formula of $AgPb(Sb,Bi)_3S_6$.

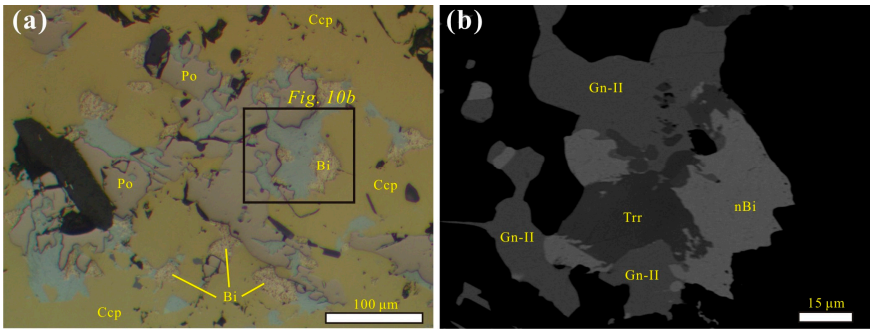

Figure 10. Reflected light photomicrograph (**a**) and back-scattered electron image (**b**) of terrywallaceite. (**a**) Terrywallaceite (Trr) with galena II (Gn-II) and native bismuth (nBi) infill along the edge of chalcopyrite (Ccp) and pyrrhotite (Po); (**b**) enlarged BSE image of Figure 10a, showing galena II replacing terrywallaceite and native bismuth infilling terrywallaceite and chalcopyrite.

Table 5. EPMA data for terrywallaceite.

Analyses	wt %										apfu Σ11 Atoms								
	Pb	Ag	Fe	Cu	Bi	Sb	As	Se	S	Total	Pb	Ag	Fe	Cu	Bi	Sb	As	Se	S
Gn77a	20.53	9.76	0.81	0.37	41.33	8.74	0.14	1.18	18.04	100.90	1.03	0.94	0.15	0.06	2.05	0.75	0.02	0.16	5.85
Gn78a	20.13	9.86	0.82	0.27	38.93	11.29	0.17	0.70	18.72	100.89	0.99	0.93	0.15	0.04	1.89	0.94	0.02	0.09	5.94
Gn79a	21.36	10.12	0.80	0.96	30.69	16.50	0.23	0.69	19.62	100.97	1.00	0.91	0.14	0.15	1.43	1.32	0.03	0.09	5.94
Gn81a	20.47	9.90	0.15	0.04	34.82	14.24	0.23	0.59	19.41	99.84	0.99	0.92	0.03	0.01	1.68	1.18	0.03	0.08	6.09
Gn85a	21.92	10.26	0.49	0.18	27.77	19.08	0.31	0.57	20.03	100.60	1.02	0.92	0.09	0.03	1.28	1.51	0.04	0.07	6.04
Gn86a	20.29	10.22	0.42	0.61	34.44	14.30	0.20	0.64	19.09	100.20	0.98	0.95	0.08	0.10	1.65	1.18	0.03	0.08	5.96
Gn87a	20.46	9.83	1.13	0.25	36.86	12.24	0.24	0.53	19.00	100.54	0.99	0.92	0.20	0.04	1.77	1.01	0.03	0.07	5.96
Gn106a	20.41	9.66	0.42	0.40	37.59	11.71	0.17	0.96	18.74	100.05	1.01	0.91	0.08	0.06	1.84	0.98	0.02	0.12	5.97
Gn107a	24.36	9.49	0.35	0.46	27.43	17.54	0.25	1.03	19.38	100.28	1.16	0.87	0.06	0.07	1.29	1.42	0.03	0.13	5.96
Mean (n = 9)	21.38	9.80	0.58	0.43	34.08	13.95	0.21	0.79	19.05	100.27	1.04	0.91	0.10	0.07	1.64	1.15	0.03	0.10	5.96

4.2.4. Freibergite

Freibergite is abundant within the Jialong ores and occurs together with native bismuth. Freibergite grains are irregularly shaped and range from several μm to 100 μm in diameter. Texturally, freibergite is incorporated in, but formed earlier than, galena II (Figure 11). Freibergite (Table 6) contains 20.85–23.06 wt % Cu, 19.44–22.09 wt % Ag, 25.77–27.64 wt % Sb, and 23.22–24.26 wt % S, with small amounts of Fe (5.46–6.26 wt %), As (0.43–0.53 wt %) and Bi (0.15–0.26 wt %), and has an mean chemical formula of $Ag_{3.40}Cu_{6.32}Fe_{1.92}B_{0.02}Sb_{3.95}As_{0.12}S_{13.27}Se_{0.01}$.

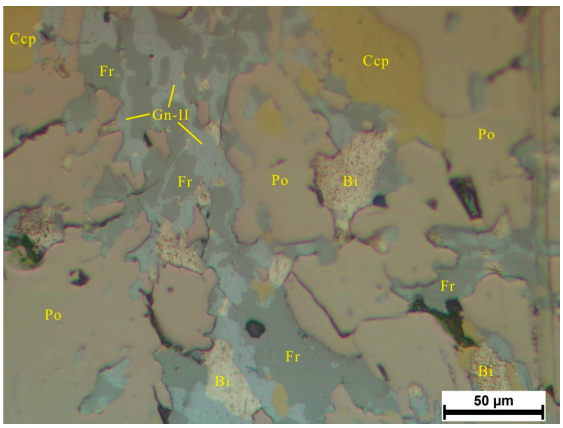

Figure 11. Reflected light photomicrograph of freibergite (Fr) associated with galena II (Gn-II) and native bismuth (Bi), infilling cavities between pyrrhotite (Po) crystals and partially replacing them. The image shows freibergite grains enclosed by galena II.

Table 6. EPMA data for freibergite.

Analyses	wt %										apfu Σ29 Atoms								
	Cu	Ag	Fe	Pb	Bi	Sb	As	Se	S	Total	Cu	Ag	Fe	Pb	Bi	Sb	As	Se	S
Yc9	22.65	19.48	5.89	0.12	0.26	25.94	0.51	0.05	23.76	98.65	6.44	3.26	1.90	0.01	0.02	3.85	0.12	0.01	13.38
Yc17	22.98	19.44	5.99	0.05	0.22	25.77	0.43	0.05	23.33	98.26	6.57	3.27	1.95	0.00	0.02	3.85	0.10	0.01	13.22
Gn94a	21.40	22.09	6.26	0.06	0.20	25.65	0.48	-	23.57	99.71	6.08	3.70	2.02	0.00	0.02	3.80	0.12	-	13.27
Gn95a	20.85	21.96	5.99	-	0.16	27.31	0.50	0.06	23.51	100.33	5.93	3.68	1.94	-	0.01	4.05	0.12	0.01	13.25
Yc11	22.93	19.29	6.02	-	0.09	26.08	0.53	0.04	23.51	98.48	6.53	3.24	1.95	-	0.01	3.87	0.13	0.01	13.27
Yc14	22.39	20.15	5.78	0.03	0.17	27.64	0.48	-	23.43	100.08	6.36	3.37	1.87	0.00	0.01	4.09	0.12	-	13.18
Yc13	21.99	20.37	5.46	0.07	0.15	27.33	0.51	-	23.22	99.10	6.32	3.45	1.78	0.01	0.01	4.10	0.12	-	13.21
Yc16	21.82	20.44	6.05	-	0.15	27.51	0.48	0.03	23.54	100.02	6.19	3.42	1.95	-	0.01	4.07	0.12	0.01	13.23
Yc16	22.03	20.72	6.19	0.02	0.24	25.40	0.51	-	23.44	98.56	6.29	3.49	2.01	0.00	0.02	3.79	0.12	-	13.27
Yc18	23.06	19.94	5.91	0.11	0.20	27.56	0.44	0.05	24.26	101.53	6.40	3.26	1.87	0.01	0.02	3.99	0.10	0.01	13.34
Yc17	22.53	19.80	5.77	-	0.16	27.29	0.52	0.04	23.73	99.84	6.37	3.30	1.86	-	0.01	4.03	0.12	0.01	13.30
Mean (n = 11)	22.24	20.33	5.94	0.07	0.18	26.68	0.49	0.05	23.57	99.50	6.32	3.40	1.92	0.01	0.02	3.95	0.12	0.01	13.27

"-" below detection limits.

4.2.5. Ullmannite

Ullmannite is scarce in the Jialong ore samples and occurs with galena II and native bismuth in the interstices of pyrrhotite crystals (Figure 12). Ullmannite has a higher reflectance than galena and a lower hardness than pyrrhotite. The analyses shows amounts of 0.42–0.87 wt % Fe, 0.43–1.64 wt % Bi, 1.01–1.16 wt % As and 0.20–0.40 wt % Se (Table 7), with an average chemical formula of $Ni_{0.97}Fe_{0.02}Sb_{0.97}As_{0.03}Bi_{0.01}S_{1.00}Se_{0.01}$.

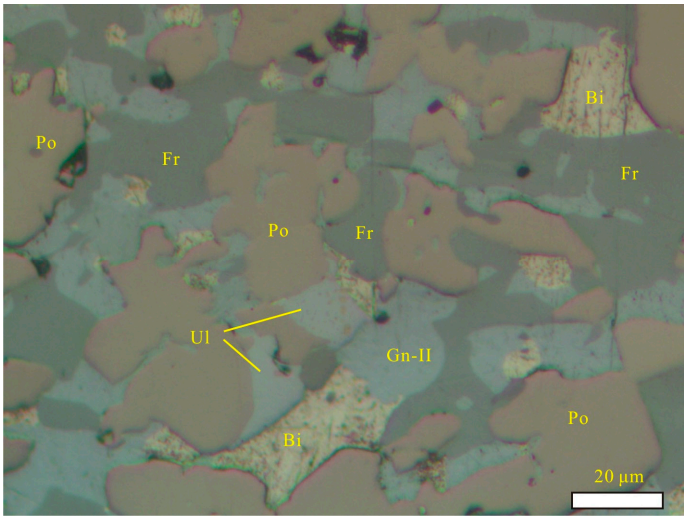

Figure 12. Reflected light photomicrograph of ullmannite (Ul), showing ullmannite infill in pyrrhotite fissures (Po). Mineral abbreviation: Fr = freibergite, Gn-II = galena II, and Bi = native bismuth.

Table 7. EPMA data for ullmannite.

Analyses	wt %									apfu Σ3 Atoms							
	Ni	Fe	Zn	Bi	Sb	As	S	Se	Total	Ni	Fe	Zn	Bi	Sb	As	S	Se
Gn89a	27.41	0.54	0.06	0.47	56.46	1.13	15.08	0.24	101.40	0.98	0.02	0.00	0.00	0.97	0.03	0.99	0.01
Gn92d	26.53	0.42	0.08	0.43	56.06	1.07	15.04	0.20	99.82	0.96	0.02	0.00	0.00	0.98	0.03	1.00	0.01
Gn90a	26.89	0.87	-	1.64	55.80	1.13	15.18	0.40	101.89	0.96	0.03	-	0.02	0.96	0.03	0.99	0.01
Gn92b	27.22	0.56	-	0.53	53.89	1.16	15.26	0.35	98.99	0.98	0.02	-	0.01	0.94	0.03	1.01	0.01
Gn92a	26.47	0.45	0.07	0.69	56.04	1.01	15.03	0.26	100.03	0.96	0.02	0.00	0.01	0.98	0.03	1.00	0.01
Mean (n = 5)	26.90	0.57	0.07	0.75	55.65	1.10	15.12	0.29	100.43	0.97	0.02	0.00	0.01	0.97	0.03	1.00	0.01

"-" below detection limits.

4.2.6. Bournonite

Bournonite is a common sulphosalt in the Jialong ores with a variable size from several μm to more than 300 μm. Texturally, grain contacts of bournonite are infilled by tintinaite, galena I, and Sb-Bi alloys (Figure 13). According to the EPMA data, the mineral contains 40.29–41.27 wt % Pb, 12.02–13.18 wt % Cu, 23.14–24.56 wt % Sb, and 19.84–20.69 wt % S, with trace amounts of Bi (0.72–1.17 wt %), Fe (0.15–1.10 wt %), As (0.33–0.44 wt %) and Se (0.43–0.77 wt %) (Table 8), and an average chemical formula of $Pb_{0.95}Cu_{0.96}Fe_{0.04}Bi_{0.02}Sb_{0.94}As_{0.02}S_{3.03}Se_{0.04}$.

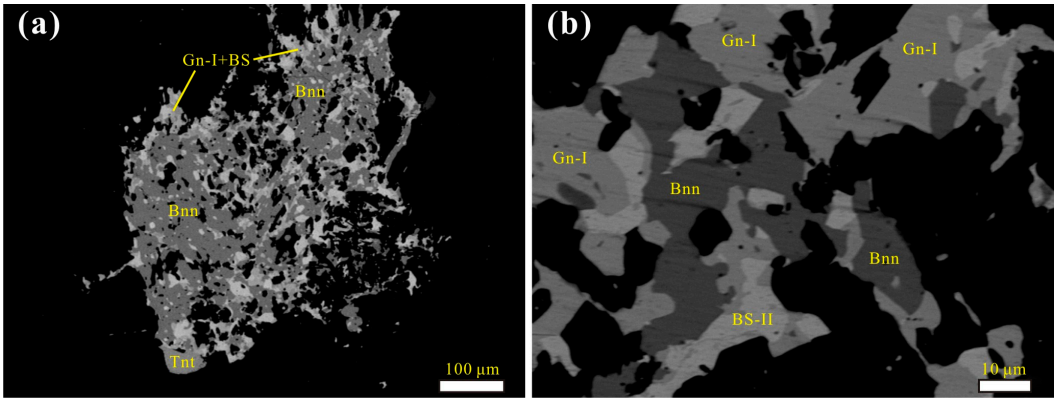

Figure 13. Back-scattered electron images of bournonite and associated minerals. (**a**) Bournonite (Bnn) infilled by Sb-Bi alloys and galena I along edges and internal fissures; and (**b**) irregular bournonite replaced or infilled by galena I and Sb-Bi alloys.

Table 8. EPMA data for bournonite.

Analyses	wt %										apfu Σ6 Atoms								
	Pb	Bi	Cu	Fe	Ag	Sb	As	S	Se	Total	Pb	Bi	Cu	Fe	Ag	Sb	As	S	Se
Gn9a	41.27	1.05	12.56	0.36	-	23.62	0.41	19.90	0.77	99.92	0.97	0.02	0.96	0.03	-	0.94	0.03	3.01	0.05
Gn10a	40.86	0.81	12.73	0.39	-	23.39	0.34	19.84	0.68	99.04	0.96	0.02	0.98	0.03	-	0.94	0.02	3.01	0.04
Gn11a	40.32	0.91	13.18	0.27	-	23.19	0.33	19.93	0.57	98.69	0.95	0.02	1.01	0.02	-	0.93	0.02	3.02	0.03
Gn17a	40.29	1.17	12.02	1.10	-	23.32	0.36	20.39	0.63	99.27	0.93	0.03	0.91	0.09	-	0.92	0.02	3.05	0.04
Gn51a	41.17	0.72	12.67	0.88	-	23.14	0.44	20.69	0.58	100.29	0.94	0.02	0.95	0.07	-	0.90	0.03	3.06	0.03
Gn52a	41.08	0.94	12.21	0.20	-	25.15	0.37	20.65	0.69	101.28	0.94	0.02	0.91	0.02	-	0.98	0.02	3.06	0.04
Gn54a	40.76	1.15	13.09	0.15	-	24.56	0.42	20.01	0.43	100.57	0.95	0.03	0.99	0.01	-	0.97	0.03	3.00	0.03
Gn56a	40.78	1.15	13.03	0.28	-	24.47	0.36	19.93	0.52	100.54	0.95	0.03	0.99	0.02	-	0.97	0.02	2.99	0.03
Mean (8)	40.81	0.99	12.69	0.45	-	23.86	0.38	20.17	0.61	99.95	0.95	0.02	0.96	0.04	-	0.94	0.02	3.03	0.04

"-" below detection limits.

4.3. Associated Sulphides and Rare Minerals

Other minerals associated with Sb-Bi alloys and sulphosalts are galena, gudmundite bismuthinite (Bi_2S_3), unnamed (BiS), and scarce nisbite.

4.3.1. Galena

Galena is widely distributed in the Jialong ore samples and mostly comprises anhedral grains ranging from several to tens of micrometres. According to mineral assemblages and chemical compositions, two types of galena are identified (galena I and galena II). Galena I is intergrown with Sb-Bi alloys and contains 0.30–0.47 wt % Bi and 0.87–1.49 wt % Se, while galena II occurs with bismuthinite and native bismuth, and contains 1.66–2.80 wt % Bi and 1.92–3.14 wt % Se (Table 9). In addition, galena II has more Ag than galena I. The data show some substitutions of Bi and Ag for 2 Pb.

Table 9. EPMA data for galena.

Analyses	wt %									apfu ∑2 Atoms							
	Pb	Fe	Cu	Ag	Bi	Sb	Se	S	Total	Pb	Fe	Cu	Ag	Bi	Sb	Se	S
Galena I																	
G13	84.09	0.18	0.25	0.06	0.36	-	1.42	13.48	99.84	0.95	0.01	0.01	0.00	0.00	-	0.04	0.98
G14	83.68	0.38	0.19	0.06	0.47	-	1.37	13.73	99.88	0.94	0.02	0.01	0.00	0.01	-	0.04	0.99
G15	84.32	0.63	-	0.12	0.47	-	1.48	13.57	100.59	0.94	0.03	-	0.00	0.01	-	0.04	0.98
G16	83.88	0.29	0.13	0.10	0.42	0.07	1.49	13.71	100.09	0.94	0.01	0.00	0.00	0.00	0.00	0.04	0.99
G39	84.63	0.44	-	-	0.31	-	1.35	13.27	100.00	0.96	0.02	-	-	0.00	-	0.04	0.97
G45	84.43	0.27	0.18	0.08	0.33	-	1.33	13.24	99.86	0.96	0.01	0.01	0.00	0.00	-	0.04	0.97
G46	84.87	0.23	-	0.17	0.30	-	0.87	13.87	100.31	0.95	0.01	0.00	0.00	0.00	-	0.03	1.01
Mean (n = 7)	84.27	0.35	0.19	0.10	0.38	0.07	1.33	13.55	100.20	0.95	0.01	0.01	0.00	0.00	0.00	0.04	0.98
Galena II																	0.99
G2	81.69	-	0.18	0.96	2.11	-	2.27	13.09	100.30	0.92	-	0.01	0.02	0.02	-	0.07	0.96
G4	80.05	-	-	1.16	2.80	-	3.14	12.64	99.79	0.92	-	-	0.03	0.03	-	0.09	0.93
G5	79.17	0.08	-	1.13	2.71	-	2.74	12.72	98.55	0.91	0.00	-	0.02	0.03	-	0.08	0.95
G6	82.09	0.50	0.13	0.85	1.66	-	2.11	13.14	100.48	0.92	0.02	0.00	0.02	0.02	-	0.06	0.95
G7	82.68	0.74	0.20	0.60	1.82	-	1.92	13.33	101.29	0.92	0.03	0.01	0.01	0.02	-	0.06	0.96
G8	82.40	0.36	0.17	0.84	2.03	-	2.31	12.99	101.10	0.93	0.02	0.01	0.02	0.02	-	0.07	0.94
G9	82.61	0.27	0.25	0.70	1.45	-	2.01	13.48	100.77	0.92	0.01	0.01	0.01	0.02	-	0.06	0.97
G10	82.03	0.77	0.21	0.89	1.95	-	2.13	13.41	101.39	0.90	0.03	0.01	0.02	0.02	-	0.06	0.95
G76	82.82	0.54	0.06	0.79	1.88	-	2.14	13.12	101.35	0.93	0.02	0.00	0.02	0.02	-	0.06	0.95
G82	81.84	0.88	0.05	0.80	1.84	-	2.33	12.93	100.67	0.92	0.04	0.00	0.02	0.02	-	0.07	0.94
G88	80.72	0.72	0.20	0.81	1.90	-	2.22	13.14	99.71	0.91	0.03	0.01	0.02	0.02	-	0.07	0.95
Mean (n = 11)	81.65	0.54	0.16	0.87	2.01	-	2.30	13.09	100.62	0.92	0.02	0.01	0.02	0.02	-	0.07	0.95

"-" below detection limits.

4.3.2. Gudmundite

Gudmundite is rarely distributed in the Jialong ore samples. The euhedral grains up to 150 μm are enclosed by quartz or are located at the grain boundaries of arsenopyrite and gangue minerals (Figure 14). Gudmundite contains 26.20–27.66 wt % Fe, 56.07–57.06 wt % Sb, 15.67–16.17 wt % S, and trace Pb (<0.02–0.05 wt %), Cu (<0.03–0.08 wt %), Bi (<0.05–0.36 wt %), and Se (<0.04–0.11 wt %) (Table 10), with an average chemical formula of $Fe_{1.00}Sb_{0.96}S_{1.03}$.

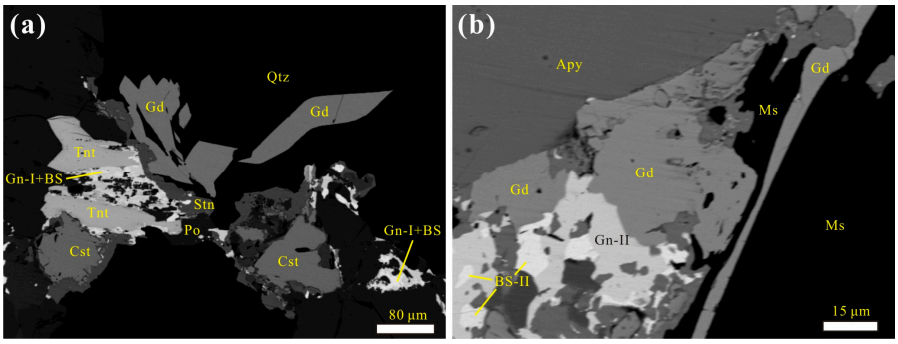

Figure 14. Back-scattered electron images of gudmundite. (**a**) Euhedral to subhedral gudmundite grains (Gd) enclosed by quartz (Qtz); (**b**) gudmundite infills cavities between arsenopyrite (Apy) and muscovite (Ms) or cleavage planes of muscovite, and is infilled by galena I (Gn-II).

4.3.3. Bismuthinite and Unnamed BiS

Bismuthinite is associated with native bismuth, galena II, bismuthinite and unnamed BiS, all of which appear filling cavities between chalcopyrite and gangue minerals (Figure 15). Galena II, bismuthinite, and unnamed BiS have similar reflectance values (Figure 15). Based on BSE images, the paragenetic sequence of sulphides is: chalcopyrite→bismuthinite→galena II→unnamed BiS→native bismuth. (Figure 15b). The bismuthinite grains, around 40 μm in size, are incorporated in galena II, and fissures in bismuthinite are filled by native bismuth. The bismuthinite contains trace amounts of

Cu (0.03–0.32 wt %), Fe (<0.02–0.11 wt %), and Se (0.08–0.19 wt %), with an average chemical formula of $Bi_{1.89}Cu_{0.01}S_{3.09}Se_{0.01}$ (Table 11). Unnamed BiS is subhedral with grains of 10–30 µm, and formed earlier than native bismuth (Figure 15b). Unnamed BiS contains 87.26–89.10 wt % Bi, 11.12–11.36 wt % S, and trace amounts of Fe (<0.02–0.10 wt %), Cu (<0.02–0.15 wt %), and Se (<0.02–0.09 wt %) (Table 11), with an average chemical formula of $Bi_{1.09}S_{0.90}$. The Bi:S ratio is close to 1:1.

Table 10. EPMA data for gudmundite.

Analyses	wt %									apfu Σ3 Atoms							
	Fe	Pb	Cu	Bi	Ag	Sb	Se	S	Total	Fe	Pb	Cu	Bi	Ag	Sb	Se	S
Gn19	27.66	-	-	-	-	56.16	0.07	16.17	100.07	1.02	-	-	-	-	0.95	0.00	1.04
Gn20	27.14	-	0.04	0.06	-	56.95	-	15.93	100.11	1.00	-	0.00	0.00	-	0.97	-	1.03
Gn21	27.42	-	0.03	0.17	-	56.46	-	15.98	100.06	1.01	-	0.00	0.00	-	0.96	-	1.03
Gn22	27.38	-	0.05	0.36	0.04	56.28	0.11	16.04	100.25	1.01	-	0.00	0.00	0.00	0.95	0.00	1.03
Gn25	27.59	0.05	0.08	-	-	56.99	-	16.04	100.75	1.01	0.00	0.00	-	-	0.96	-	1.03
Gn47	26.33	0.02	-	-	-	57.06	0.04	15.67	99.12	0.99	0.00	-	-	-	0.98	0.00	1.03
Gn48	26.47	-	-	-	-	56.73	-	15.78	98.98	0.99	-	-	-	-	0.98	-	1.03
Gn49	26.20	0.04	-	-	-	56.07	-	15.73	98.04	0.99	0.00	-	-	-	0.97	-	1.04
Mean (n = 8)	27.02	0.04	0.05	0.20	0.04	56.59	0.07	15.92	99.91	1.00	0.00	0.00	0.00	0.00	0.96	0.00	1.03

"-" below detection limits.

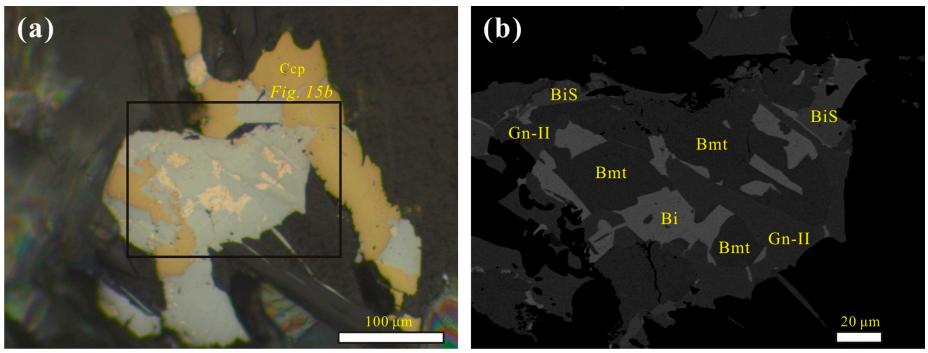

Figure 15. Reflected light photomicrograph (**a**) and BSE image (**b**) of the mineral association of native bismuth (Bi), galena II (Gn-II), bismuthinite (Bmt) and the unnamed BiS mineral, which appears filling cavities between chalcopyrite (Ccp) and gangue minerals.

Table 11. EPMA data for bismuthinite and unnamed BiS.

Analyses	wt %						apfu Σ3 Atoms				
	Cu	Fe	Bi	Se	S	Total	Cu	Fe	Bi	Se	S
	Bismuthinite						∑5 atoms				
Gn98	0.16	0.02	80.27	0.12	20.15	100.72	0.01	0.00	1.89	0.01	3.09
Gn99	0.17	-	80.91	0.15	20.05	101.28	0.01	-	1.90	0.01	3.07
Gn100	0.11	0.06	80.09	0.13	20.04	100.43	0.01	0.01	1.89	0.01	3.09
Gn102	0.22	0.11	79.66	0.17	20.08	100.24	0.02	0.01	1.88	0.01	3.08
Gn103	0.10	0.04	80.41	0.18	20.41	101.14	0.01	0.00	1.88	0.01	3.10
Gn104	0.03	0.05	80.43	0.19	20.06	100.76	0.00	0.00	1.90	0.01	3.08
Gn105	0.32	0.02	79.62	0.08	20.30	100.34	0.02	0.00	1.87	0.00	3.10
Gn106	0.18	0.05	80.58	0.08	19.97	100.86	0.01	0.00	1.90	0.01	3.07
Mean (n = 8)	0.16	0.05	80.25	0.14	20.13	100.73	0.01	0.00	1.89	0.01	3.09
	Unnamed BiS						apfu ∑2 atoms				
Gn96a	0.15	-	88.71	0.06	11.36	100.28	0.01	-	1.09	0.00	0.91
Gn107	0.11	0.02	88.31	0.09	11.21	99.74	0.00	0.00	1.09	0.00	0.90
Gn108	0.04	-	89.10	0.06	11.16	100.36	0.00	-	1.10	0.00	0.90
Gn109	0.14	0.10	88.55	0.05	11.51	100.35	0.01	0.00	1.08	0.00	0.91
Gn110	-	-	88.34	0.08	11.12	99.54	-	-	1.10	0.00	0.90
Gn111	-	0.06	87.26	-	11.34	98.66	-	0.00	1.08	-	0.92
Mean (n = 6)	0.11	0.06	88.38	0.07	11.28	99.90	0.00	0.00	1.09	0.00	0.90

"-" below detection limits.

4.3.4. Nisbite

Nisbite is a trace mineral in the Jialong ores that coexists with Sb-Bi alloys and native bismuth. It occurs as small grains of 3–20 μm in diameter. Nisbite is surrounded by native bismuth, galena (I or II) or Sb-Bi alloys in complex aggregates that infill interstitial cavities between pyrrhotite grains. The pyrrhotite is partially corroded and infilled by native bismuth (Figure 16a), which also infills galena I and Sb-Bi alloys (Figure 16b). Nisbite contains 18.41–19.46 wt % Ni and 77.70–79.82 wt % Sb with trace amounts of Fe (0.75–2.03 wt %) (Table 12), and an average chemical formula of $Ni_{0.99}Fe_{0.09}Sb_{1.90}S_{0.02}$.

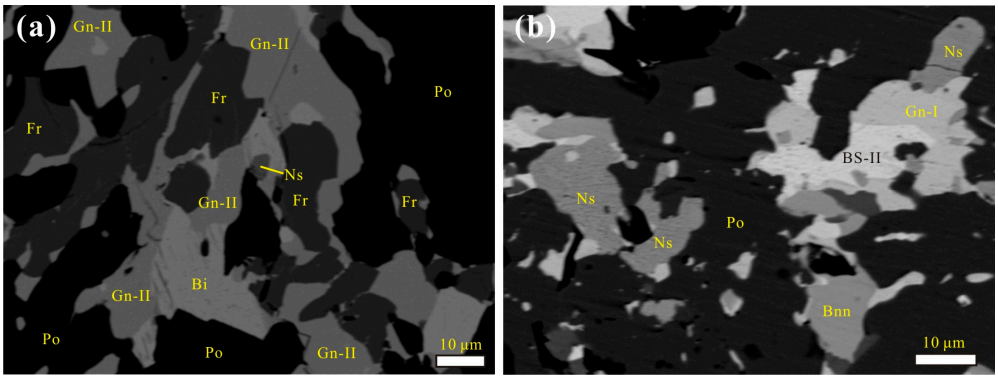

Figure 16. Back-scattered electron images of nisbite. (**a**) Fine nisbite (Ns) incorporated in native bismuth (Bi); (**b**) nisbite filling pyrrhotite (Po) fissures and infilled by galena I (Gn-I). Mineral abbreviation: Fr = freibergite, Bnn = bournonite, BS-II = Phase II of Sb-Bi alloys.

Table 12. EPMA data for nisbite.

Analyses	wt %								apfu Σ3 Atoms						
	Ni	Fe	Zn	Sb	Bi	S	Se	Total	Ni	Fe	Zn	Sb	Bi	S	Se
Gn93	18.88	0.83	0.13	79.70	0.21	0.20	0.06	100.00	0.96	0.04	0.01	1.96	0.00	0.02	0.00
Ns1	19.10	1.45	-	79.82	-	0.17	-	100.54	0.96	0.08	-	1.94	-	0.02	-
Ns2	18.81	1.95	0.04	77.82	0.08	0.25	-	98.94	0.96	0.10	0.00	1.91	0.00	0.02	-
Ns3	19.46	0.75	-	79.03	-	0.13	-	99.37	1.00	0.04	-	1.95	-	0.01	-
Ns4	18.41	2.03	0.22	77.71	-	0.36	0.08	98.81	0.94	0.11	0.01	1.91	-	0.03	0.00
Mean (n = 5)	18.93	1.40	0.13	78.82	0.14	0.22	0.07	99.71	0.96	0.07	0.01	1.93	0.00	0.02	0.00

"-" below detection limits.

5. Discussion

5.1. Compositional Variations of the Sb-Bi Alloys

Native bismuth is widely distributed in various deposits, e.g., W-Sn deposits [7,16,27,28], Pb-Zn deposits [29–31], and Au deposits [4,32–36]. On the other hand, native Sb is less common and occurs mostly in Au-Sb or Au deposits [37–40], and in trace amounts in Pb-Zn deposits [41,42] and Sn-polymetallic deposits [43]. However, Sb-Bi alloys are rarely reported in deposits [15]. Previous studies have shown that, in geological processes, small amounts of bismuthian antimony [15,17,18] or antimonian bismuth [13,15,19] are formed. Only trace amounts of antimonian bismuth (containing 1.5–13.8 wt % Sb) and bismuthian antimony (containing 13.4 wt % Bi) are present in the Tanco pegmatite in Canada [15].

The Jialong is a rare deposit containing a high abundance of Sb-Bi alloys. The Sb-Bi alloys contain variable Sb and Bi contents ranging from 20.72 wt % to 98.89 wt % Bi and 0.89 wt % to 77.68 wt % Sb. Two phases of Sb-Bi alloys separated by a composition gap are identified (Figure 17a). However, thermodynamic calculations show that Sb-Bi solid solution is a continuous solution [44] that includes the compositions of Phase I and Phase II (Figure 17b). The crystallisation temperature during cooling

is higher for Phase I (Sb-rich member) than Phase II (Bi-rich member) (Figure 17b). Phase I is formed earlier than Phase II according to textural analysis (Figure 5c); the earlier formation also indicates higher formation temperatures for Phase I. Because continuous slow cooling would precipitate the full range of solid solutions, the presence of two phases implies multiple steps of non-continuous temperature decrease during formation.

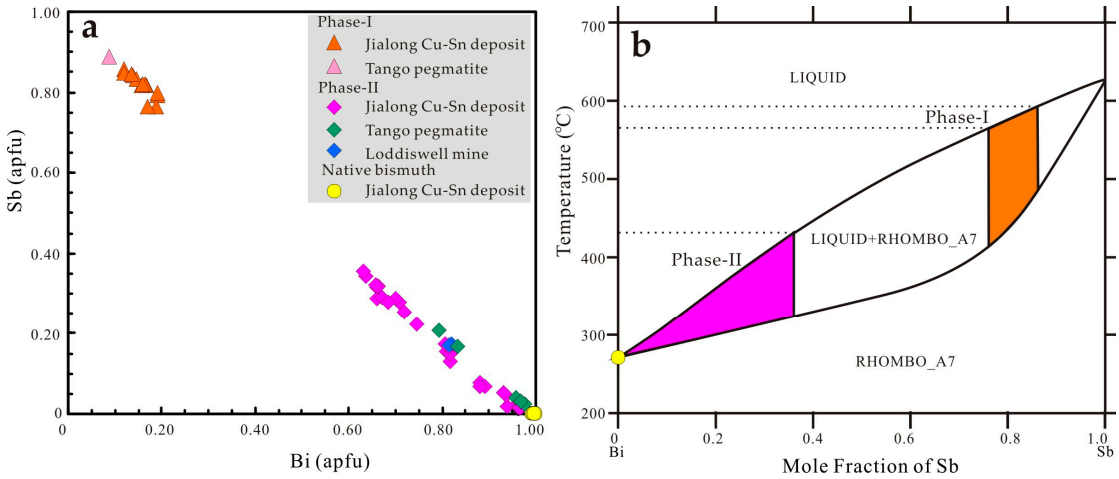

Figure 17. (**a**) In a Diagram of Bi (apfu) versus Sb (apfu) for the Sb-Bi alloys (Phase I and Phase II) showing the compositional gap between them. The data of the Loddiswell mine and the Tanco pegmatite are from [14,15], respectively; (**b**) Sb-Bi phase diagram (after [45,46]), showing the temperature and composition gap between Phase I and Phase II. Note that the temperatures that stabilise the Sb-Bi alloys in the pure Sb-Bi system in laboratory conditions are higher than those for the natural metallogenic system.

5.2. Formation of Sb-Bi Alloys and Sulphosalts during Mineralisation

The Cu-Sn orebodies in the Jialong deposit are located in the external contact zone of the Yuanbaoshan granitic intrusion. All orebodies are less than 600 m from the intrusion boundary. They strike northwest and are controlled by faults. Some studies suggest that ore genesis is related to the presence of ultramafic rocks [47–50] in the JYR. However, because the orebodies are present in the contact zone of granite intrusions, the genesis of the Cu-Sn mineralisation system is linked to the granite intrusions [21,22,51].

The analysis of ore petrology in this study indicates that the Jialong deposit experienced four mineralisation stages. The Sb-Bi alloys and sulphosalts were formed in Stage III, and infilled cavities in chalcopyrite and pyrrhotite, while bismuthinite, unnamed BiS, and native bismuth formed in Stage IV. Our petrographic evidence shows that the Sb-Bi minerals were formed during the late stages of magmatic hydrothermal evolution. This situation is consistent with studies on other Sb-Bi mineral-bearing deposits [7]. In addition, Sb-Bi alloys are not intergrown with bismuthinite, unnamed BiS, or native bismuth in the Jialong deposit, which implies that Sb-Bi alloys and native bismuth were formed at different times.

The Sb-Bi phase diagram shows that the formation temperature of Sb-Bi alloys is higher than that of native bismuth (Figure 17b). Experiments and evidence from many geological deposits indicate that Bi sulphosalts formed at temperatures of >400–300 °C [1,4,9], while native bismuth and bismuthinite formed below 271 °C. Thus, sulphosalts and Sb-Bi alloys formed at temperatures of 271 to >400 °C.

Additional evidence shows that the Bi-bearing galena in Stages III and IV formed at higher temperatures than pure galena [1]. Sb-Bi mineral precipitation is affected by temperature, sulphur fugacity, oxygen fugacity, pH, and the solubility of Bi and Sb ions [7]. The precipitation of many sulphides and sulphosalts during the late third stage depleted the fluid of S. This low f_{S2} fluid could

then precipitate Sb-Bi alloys and trace amounts of nisbite at high temperature. After formation of Sb-Bi alloys, a later mineralisation stage formed bismuthinite, galena II, unnamed BiS, and native bismuth. The formation of additional sulphur minerals indicates that the fourth stage experienced decreasing f_{S2}, which could support the deposition of native bismuth at lower temperature.

6. Conclusions

(1) The Sb-Bi alloys in the Jialong Cu-Sn deposit are 1–20 μm and intergrown with earlier-formed sulphosalts. The alloys formed during the late stages of hydrothermal mineralisation.

(2) Seven sulphosalts were identified in the Jialong deposit, including Bi sulphosalt (pavonite), Sb-Bi sulphosalts (tintinaite and terrywallaceite), and Sb sulphosalts (freibergite, ullmanite, bournonite).

(3) Two phases of Sb-Bi alloys were identified. The textural relationship indicate that Phase I was formed before Phase II. The composition of Phase I is dominated by Sb, while that of Phase II is dominated by Bi. It is inferred that Sb-Bi alloys formed in a high temperature (271–400 °C) and low f_{S2} environment. The presence of the two phases may indicate multiple steps of cooling during mineralisation.

(4) The Jialong deposit is related to granite intrusions. Sulphosalts, Sb-Bi alloys, bismuthinite, and native bismuth were precipitated from the late Sb-Bi-rich fluid during cooling and fluctuating f_{S2} conditions.

Acknowledgments: This work was jointly supported by the National Natural Science Foundation of China (Grant 41302048) and the Innovation-driven Plan of Central South University (Grant 2015CX008). Jeffrey M. Dick of Central South University is thanked for English polishing.

Author Contributions: Jianping Liu, Weikang Chen, and Qingquan Liu conceived and designed the experiments; Weikang Chen performed the experiments; all authors wrote the paper.

Conflicts of Interest: The authors declare no conflict of interest.

References

1. Kołodziejczyk, J.; Pršek, J.; Melfos, V.; Voudouris, P.C.; Maliqi, F.; Kozub-Budzyń, G. Bismuth minerals from the Stan Terg deposit (Trepça, Kosovo). *Neues Jahrb. Mineral. Abh.* **2015**, *192*, 317–333. [CrossRef]
2. Moelo, Y.; Roger, G.; Maurel-Palacin, D.; Marcoux, E.; Laroussi, A. Chemistry of some Pb-(Cu, Fe)-(Sb, Bi) sulfosalts from France and Portugal. Implications for the crystal chemistry of lead sulfosalts in the Cu-poor part of the Pb_2S_2–Cu_2S-Sb_2S_3–Bi_2S_3 system. *Mineral. Petrol.* **1995**, *53*, 229–250. [CrossRef]
3. Paar, W.H.; Chen, T.T. Meixner, H. Pb-Bi-(Cu)-Sulfosalts in Paleozoic Gneisses and Schists from Oberpinzgau, Salzburg Province, Austria. *TMPM Tschermaks Miner. Petrogr. Mitt.* **1980**, *27*, 1–16. [CrossRef]
4. Fuertes-Fuente, M.; Cepedal, A.; Lima, A.; Dória, A.; Ribeiro, M.A.; Guedes, A. The Au-bearing vein system of the Limarinho Deposit (Northern Portugal): Genetic constraints from Bi-chalcogenides and Bi-Pb-Ag sulfosalts, fluid inclusions and stable isotopes. *Ore Geol. Rev.* **2016**, *72*, 213–231. [CrossRef]
5. Cook, N.J. Bismuth and bismuth-antimony sulphosalts from Neogene vein mineralisation, Baia Borsa area, Maramures, Romania. *Miner. Mag.* **1997**, *61*, 387–409. [CrossRef]
6. Voudouris, P.C.; Spry, P.G.; Mavrogonatos, C.; Sakellaris, G.A.; Bristol, S.K.; Melfos, V.; Fornadel, A.P. Bismuthinite derivatives, lillianite homologues, and bismuth sulfotellurides as indicators of gold mineralization in the Stanos shear-zone related deposit, Chalkidiki, Northern Greece. *Can. Mineral.* **2013**, *51*, 119–142. [CrossRef]
7. Zhang, L.; Wen, H.; Qin, C.; Du, S.; Zhu, C.; Fan, H.; Zhang, J. The geological significance of Pb-Bi- and Pb-Sb-sulphosalts in the Damajianshan tungsten polymetallic deposit, Yunnan Province, China. *Ore Geol. Rev.* **2015**, *71*, 203–214. [CrossRef]
8. Radosavljević, S.A.; Stojanović, J.N.; Pačevski, A.M. Radosavljević-Mihajlović, A.S.; Kašić, V.D. A review of Pb-Sb(As)-S, Cu(Ag)-Fe(Zn)-Sb(As)-S, Ag(Pb)-Bi(Sb)-S and Pb-Bi-S(Te) sulfosalt systems from the Boranja orefield, West Serbia. *Geol. Anali Balk. Poluos.* **2016**, *77*, 1–12.
9. Buzatu, A.; Damian, G.; Dill, H.G.; Buzgar, N.; Apopei, A.I. Mineralogy and geochemistry of sulfosalts from Baia Sprie ore deposit (Romania)—New bismuth minerals occurrence. *Ore Geol. Rev.* **2015**, *65*, 132–147. [CrossRef]

10. Hawley, J.E.; Berry, L.G. Michenerite and froodite, palladium bismuth minerals. *Can. Mineral.* **1958**, *6*, 200–209.
11. Stolyarova, T.A.; Voronin, M.V.; Osadchii, E.G.; Brichkina, E.A. Enthalpy of formation of palladium bismuthides PdBi and $PdBi_2$ from elements. *Geochem. Int.* **2015**, *53*, 748–751. [CrossRef]
12. Novoselov, K.; Belogub, E.; Kotlyarov, V.; Mikhailov, A. Ore mineralogy and formation conditions of the Pirunkoukku gold occurrence (Finland). *Eur. J. Mineral.* **2015**, *27*, 639–649. [CrossRef]
13. Kozhemyakin, G.N.; Nalivkin, M.A.; Rom, M.A.; Mateychenko, P.V. Growing Bi-Sb gradient single crystals by a modified Czochralski method. *J. Cryst. Growth* **2004**, *263*, 148–155. [CrossRef]
14. Stanley, C.J.; Halls, C.; Camm, G.S.; James, J. Gold–antimony mineralization at Loddiswell, Devon, UK. *Terra Nova* **1990**, *2*, 224–231. [CrossRef]
15. Cerny, P.; Harris, D.C. The tanco pegmatite at Bernic Lake, Manitoba. Xi. Native elements, alloys, sulfides and sulfosalts. *Can. Mineral.* **1978**, *16*, 625–640.
16. Gvozdev, V.I. Bismuth mineralization in ores of the Skrytoe scheelite deposit (Primorye) and problems of its genesis. *Russ. J. Pac. Geol.* **2009**, *3*, 69–79. [CrossRef]
17. Sejkora, J.; Berlepsch, P.; Makovicky, E.; Balic-Zunic, T.; Litochleb, J. Teallite from Radvanice near Trutnov (Czech Republic). *Neues Jahrb. Mineral. Abh.* **2002**, *177*, 163–180. [CrossRef]
18. Volborth, A. Gediegen Wismutantimon und andere Erzmineralien im Li-Be-Pegmatit von Viitaniemi, Eriijiirvi, Zentral Finnland. *N. Jahrb. Mineral. Abh.* **1960**, *94*, 140–149.
19. Cook, N.J. Mineralogy of the sulphide deposits at Sulitjelma, northern Norway. *Ore Geol. Rev.* **1996**, *11*, 303–338. [CrossRef]
20. Huang, C. *Geological Report of the Jialong Cu-Sn Deposit in Baiyun Town, Rongshui County, Guangxi Zhuang Autonomous Region*; Bureau of Geology and mineral resources of Guangxi Zhuang Autonomous Region: Nanning, China, 1972; pp. 1–32. (In Chinese)
21. Mao, J. Geological features and minerogenic series of the tin polymetallic deposits in Jiuwandashan–Yuanbaoshan area, Northern Guangxi. *Miner. Depos.* **1987**, *6*, 22–32. (In Chinese)
22. Mao, J. Tourmalinite from northern Guangxi, China. *Miner. Depos.* **1995**, *30*, 235–245.
23. BGMRGX (Bureau of Geology and Mineral Resources of Guangxi Province). *Regional Geology of Guangxi Autonomous Region*; Geological Publishing House: Beijing, China, 1985; pp. 1–853. (In Chinese)
24. Wang, X.; Zhou, J.; Qiu, J.; Zhang, W.; Liu, X.; Zhang, G. Petrogenesis of the Neoproterozoic strongly peraluminous granitoids from Northern Guangxi: Constraints from zircon geochronology and Hf isotopes. *Acta Petrol. Sin.* **2006**, *22*, 326–342. (in Chinese).
25. Wang, X.L.; Zhou, J.C.; Qiu, J.S.; Gao, J.F. Geochemistry of the Meso- to Neoproterozoic basic–acid rocks from Hunan Province, South China: implications for the evolution of the western Jiangnan orogen. *Precambrian Res.* **2004**, *135*, 79–103. [CrossRef]
26. Yang, H.; Downs, R.T.; Evans, S.H.; Pinch, W.W. Terrywallaceite, $AgPb(Sb,Bi)_3S_6$, isotypic with gustavite, a new mineral from Mina Herminia, Julcani Mining District, Huancavelica, Peru. *Am. Miner.* **2013**, *98*, 1310–1314. [CrossRef]
27. Sinclair, W.D.; Kooiman, G.J.A.; Martin, D.A.; Kjarsgaard, I.M. Geology, geochemistry and mineralogy of indium resources at Mount Pleasant, New Brunswick, Canada. *Ore Geol. Rev.* **2006**, *28*, 123–145. [CrossRef]
28. Seifert, T.; Sandmann, D. Mineralogy and geochemistry of indium-bearing polymetallic vein-type deposits: Implications for host minerals from the Freiberg district, Eastern Erzgebirge, Germany. *Ore Geol. Rev.* **2006**, *28*, 1–31. [CrossRef]
29. Ye, L.; Liu, T.; Yang, Y.; Gao, W.; Pan, Z.; Bao, T. Petrogenesis of bismuth minerals in the Dabaoshan Pb–Zn polymetallic massive sulfide deposit, northern Guangdong Province, China. *J. Asian Earth Sci.* **2014**, *82*, 1–9. [CrossRef]
30. Ilmen, S.; Alansari, A.; Baidada, B.; Maacha, L.; Bajddi, A. Minerals of the Ag-Bi-Cu-Pb-S system from the Amensif carbonate-replacement deposit (western High Atlas, Morocco). *J. Geochem. Explor.* **2016**, *161*, 85–97. [CrossRef]
31. Pažout, R.; Sejkora, J.; Šrein, V. Bismuth and bismuth–antimony sulphosalts from Kutná Hora vein Ag–Pb–Zn ore district, Czech Republic. *J. Geosci.* **2017**, *62*, 59–76. [CrossRef]
32. Ciobanu, C.L.; Cook, N.J.; Damian, F.; Damian, G. Gold scavenged by bismuth melts: An example from Alpine shear-remobilizates in the Highiş Massif, Romania. *Mineral. Petrol.* **2006**, *87*, 351–384. [CrossRef]

33. Zheng, B.; Zhu, Y.; An, F.; Huang, Q.; Qiu, T. As-Sb-Bi-Au mineralization in the Baogutu gold deposit, Xinjiang, NW China. *Ore Geol. Rev.* **2015**, *69*, 17–32. [CrossRef]
34. Zhou, H.; Sun, X.; Fu, Y.; Lin, H.; Jiang, L. Mineralogy and mineral chemistry of Bi-minerals and constraints on ore genesis of the Beiya giant porphyry–skarn gold deposit, southwest China. *Ore Geol. Rev.* **2016**, *79*, 408–424. [CrossRef]
35. Martínez-Abad, I.; Cepedal, A.; Arias, D.; Martín-Izard, A. The Vilalba gold district, a new discovery in the Variscan terrenes of the NW of Spain: A geologic, fluid inclusion and stable isotope study. *Ore Geol. Rev.* **2015**, *66*, 344–365. [CrossRef]
36. Cepedal, A.; Fuertes-Fuente, M.; Martín-Izard, A.; González-Nistal, S.; Rodríguez-Pevida, L. Tellurides, selenides and Bi-mineral assemblages from the Río Narcea Gold Belt, Asturias, Spain: Genetic implications in Cu–Au and Au skarns. *Mineral. Petrol.* **2006**, *87*, 277–304. [CrossRef]
37. Normand, C.; Gauthier, M.; Jebrak, M. The Quebec antimony deposit: An example of Gudmundite-native antimony mineralization in the ophiolitic mélange of the southeastern Quebec Appalachians. *Econ. Geol.* **1996**, *91*, 149–163. [CrossRef]
38. Kontak, D.J.; Horne, R.J.; Smith, P.K. Hydrothermal characterization of the West Gore Sb-Bi deposit, Meguma Terrane, Nova Scotia, Canada. *Econ. Geol.* **1996**, *91*, 1239–1262. [CrossRef]
39. Thorne, K.G.; Lentz, D.R.; Hoy, D.; Fyffe, L.R.; Cabri, L.J. Characteristics of mineralization at the main zone of the Clarence Stream gold deposit, southwestern New Brunswick, Canada: Evidence of an intrusion-related gold system in the Northern Appalachian Orogen. *Explor. Min. Geol.* **2008**, *17*, 19–49. [CrossRef]
40. An, F.; Zhu, Y. Native antimony in the Baogutu gold deposit (west Junggar, NW China): Its occurrence and origin. *Ore Geol. Rev.* **2010**, *37*, 214–223. [CrossRef]
41. Cook, N.J.; Spry, P.G.; Vokes, F.M. Mineralogy and textural relationships among sulphosalts and related minerals in the Bleikvassli Zn-Pb-(Cu) deposit, Nordland, Norway. *Miner. Depos.* **1998**, *34*, 35–56. [CrossRef]
42. Li, C.Y.; Liu, Y.P.; Zhang, Q.; Pi, D.H.; Zhang, W.L.; Chen, J. Discovery of antimony and distribution characteristics of associated elements in Huize Pb-Zn deposit. *Miner. Depos.* **2005**, *24*, 52–60. (In Chinese)
43. Huang, M.; Tang, S. *Ore Petrology on Tin Field Deposit at Dachang*; Beijing Science and Technology Press: Beijing, China, 1988; pp. 1–176. (In Chinese)
44. Yéo, D.P.; Hassam, S.; Boa, D.; Mikaelian, G.; Rogez, J. DSC investigation of phase equilibria in the Bi-Pb-Sb system. *J. Chem. Thermodyn.* **2016**, *101*, 316–322. [CrossRef]
45. Feutelais, Y.; Morgant, G.; Didry, J.R.; Schnitter, J. Thermodynamic evaluation of the system bismuth–antimony. *Calphad* **1992**, *16*, 111–119. [CrossRef]
46. Minic, D.; Dokic, J.; Cosovi, V.; Stajic-Trosic, J.; Zivkovi, D.; Dervisevi, I. Experimental investigation and thermodynamic prediction of the Bi-Sb-Zn phase diagram. *Mater. Chem. Phys.* **2010**, *122*, 108–113. [CrossRef]
47. Mao, J.; Tang, S. On the alteration of the Yidong–Wudi tin deposit in Guangxi. *Bull. Chin. Acad. Geol. Sci.* **1986**, *13*, 51–71. (In Chinese)
48. Zhu, L. Mineralization and genesis of magmatic rocks in Jiumao tin mine. *J. Guizhou Inst. Technol.* **1988**, *17*, 26–38. (In Chinese)
49. Cheng, X.; Huang, Y. Discussion on the original enrichment of tin. *Geol. Explor.* **1984**, *20*, 29–35. (In Chinese)
50. Feng, Q.; Li, Y.; Liang, B. An ancient stratabound Sn-deposit in Guangxi Province. *Geol. Explor.* **1989**, *25*, 18–22. (In Chinese)
51. Zhang, S.; Ma, D.; Lu, J.; Zhang, R.; Cai, Y.; Ding, C. Geochronology, Hf isotopic compositions and geochemical characteristics of the Pingying granite pluton in Northern Guangxi, South China, and its geological significance. *Geol. J. China Univ.* **2016**, *22*, 92–104. (In Chinese)